Journal of Applied Physics

RESEARCH ARTICLE | DECEMBER 04 2024

Study of phase decoherence in GeSn (8%) through measurements of the weak antilocalization effect

Adelaide Bradicich ; Priyanka Petluru ; Shiva Davari ; Haochen Zhao ; Siddhant Gangwal ; Chia-You Liu; Dragica Vasileska ; Yuping Zeng ; Hugh Churchill ; Jiun-Yun Li ; Michael P. Lilly ; Tzu-Ming Lu

J. Appl. Phys. 136, 214301 (2024)
https://doi.org/10.1063/5.0233728

Version of Record at:
https://doi.org/10.1063/5.0233728

Journal of Applied Physics ARTICLE pubs.aip.org/aip/jap

Study of phase decoherence in GeSn (8%) through measurements of the weak antilocalization effect

Cite as: J. Appl. Phys. **136**, 214301 (2024); doi: 10.1063/5.0233728
Submitted: 16 August 2024 · Accepted: 18 November 2024 ·
Published Online: 4 December 2024

Adelaide Bradicich,[1,2,a)] Priyanka Petluru,[2] Shiva Davari,[3] Haochen Zhao,[4] Siddhant Gangwal,[5] Chia-You Liu,[6] Dragica Vasileska,[5] Yuping Zeng,[4] Hugh Churchill,[3] Jiun-Yun Li,[6,7,8] Michael P. Lilly,[1,2] and Tzu-Ming Lu[1,2]

AFFILIATIONS

[1]Center for Integrated Nanotechnologies, Sandia National Laboratories, Albuquerque, New Mexico 87123, USA
[2]Sandia National Laboratories, Albuquerque, New Mexico 87123, USA
[3]Department of Physics, University of Arkansas, Fayetteville, Arkansas 72701, USA
[4]Department of Electrical and Computer Engineering, University of Delaware, Newark, Delaware 19716, USA
[5]School of Electrical, Computer, and Energy Engineering, Arizona State University, Tempe, Arizona 85281, USA
[6]Graduate Institute of Electronics Engineering, National Taiwan University, Taipei 10617, Taiwan
[7]Department of Electrical Engineering, National Taiwan University, Taipei 10617, Taiwan
[8]Taiwan Semiconductor Research Institute, Hsinchu 300091, Taiwan

[a)]**Author to whom correspondence should be addressed:** ambradi@sandia.gov

ABSTRACT

Alloying germanium with tin offers a means to modulate germanium's electronic structure, enabling a greater degree of control over quantum properties such as the retention of the phase or spin of the electron wave. However, the extent to which the presence of high dopant concentrations in GeSn alters these quantum behaviors is poorly understood. Here, we investigate the role of dopant concentrations on phase coherence through measurements of the weak antilocalization (WAL) effect at temperatures between 30 mK and 10 K in p-GeSn (8%) thin films, which were doped to a series of carrier densities on the order of 10^{12} cm^{-2}. Phase coherence and spin–orbit lengths were extracted from the magnetoconductivities using the 2D Hikami–Larkin–Nagaoka model. Phase coherence lengths peaked at 577, 593, and 737 nm for the low-, mid-, and high-density samples, while upper limits on the spin–orbit lengths of less than 25 nm were relatively independent of carrier density and temperature. The phase coherence lengths increased as the temperature decreased but changed only minimally with carrier density, contrary to common models of temperature-dependent inelastic scattering. Saturation of the phase coherence lengths occurred below 600 mK. Based on these findings, intrinsically generated inelastic scattering mechanisms such as two-level systems or impurity band scattering likely contribute to phase decoherence in these alloys. Our results provide insight into the inelastic scattering mechanisms of GeSn, while suggesting a need for further investigation into phase decoherence mechanisms in doped group-IV alloys.

I. INTRODUCTION

Alloying group-IV elements alters the electronic properties relative to single-element semiconductors, enabling new electronic, spintronic, and photonic applications while retaining a compatibility with conventional silicon-based architectures that is challenging in other material systems.[1–4] In recent years, germanium tin (GeSn) alloys have been of particular interest due to the presence of a bandgap crossover from an indirect to a direct gap at Sn compositions above 8 %.[5–7] Achieving such high Sn compositions necessitates out-of-equilibrium synthesis processes, as the maximum equilibrium solubility of Sn in Ge is only 1.1 %.[8] Many studies have consequently focused on developing processes to achieve high Sn content and demonstrating this bandgap crossover.[9,10] However, less is known regarding the extent to which the inclusion of Sn alters the quantum transport behavior of Ge.

Version of Record at:
https://doi.org/10.1063/5.0233728

Characterizing the spin–orbit coupling (SOC) in GeSn can provide insight into its electronic structure. SOC is the momentum-dependent interaction between moving charge carriers in an electric field and the resulting effective magnetic field.[11] Magnetotransport measurements are often used to observe SOC, as an applied magnetic field alters their energetics which results in identifiable features in magnetoconductivity. For instance, weak antilocalization, electric dipole spin resonance (EDSR), and the inverse spin Hall effect are all found in group-IV materials due to the presence of SOC.[12–15] Such observations of SOC phenomena enable the extraction of SOC length, time, or rate parameters, providing information about a material's electronic structure while pointing toward its applicability in various technologies.

The weak localization (WL) effect and weak antilocalization (WAL) effect are two related quantum phenomena found in electronic materials, including group-IV semiconductors and alloys. Weak localization occurs when time-reversed symmetric self-intersecting electronic pathways of electrons interfere constructively, decreasing the material's conductivity.[16] Similarly, weak antilocalization occurs when those self-intersecting pathways interfere destructively due to an additional Berry phase π, effectively increasing electrical conductivity.[17] For both effects, application of a magnetic field dephases the electronic pathways, and SOC parameters can be extracted from the resulting magnetoconductivity using a model suited to the electronic transport regime and symmetry of the structure.[16,18,19] Key length scales associated with WL/WAL include the carrier mean free path l_{tr}, the phase coherence length l_{φ}, which is the distance over which the phase of the electron wave is retained, and the spin–orbit length l_{so}, which is the distance over which the spin of the electron wave is retained. WAL is associated with strong SOC and short values of l_{so}.

Both WL and WAL have been observed in Ge, demonstrating changes in its electronic structure through altering its carrier density through intentional doping or gating. The strength of SOC has been shown to be tunable, as studies of strained p-Ge quantum wells exhibited a transition from WL to WAL as the samples' carrier densities were increased through gating.[17,20] Measurements comparing n-Ge and p-Ge thin films found that WL presented in n-Ge while WAL was found in p-Ge.[12] Previous studies have observed a trend of increasing carrier densities correlating with increasing phase coherence lengths, which were as long as 2.6 μm at 260 mK in one study.[17,20,21]

The temperature-dependence of phase coherence is also critical to understand, as WL and WAL in Ge have shown variation with temperature. Previous studies show that phase coherence lengths of electrons and holes in Ge follow power-law temperature-dependences, while the spin–orbit lengths remain relatively constant with temperature.[12] The temperature- and carrier-density-dependence of the phase coherence lengths were typically attributed to the presence of Nyquist inelastic carrier–carrier scattering as the dominant dephasing mechanism, which predicts strong temperature-dependence and carrier-density dependence.[22]

Similar behaviors have been found in GeSn.[23,24] However, phase coherence lengths tend to be shorter in GeSn than in Ge due to the presence of alloy scattering contributing to phase decoherence.[24] Interestingly, while Sn was predicted to produce stronger SOC in GeSn compared to Ge due to its larger atomic number, SOC has been shown to weaken with higher Sn compositions.[23] This was attributed to the presence of compressive strain in the material that causes splitting between the heavy-hole and light-hole bands.[23]

While some degree of control over quantum transport has been demonstrated through altering carrier density or composition in GeSn alloys, many questions remain regarding the complex relationships between the properties of the alloy, its environment, and their roles in altering their electronic structure and consequently quantum transport behaviors. Importantly, it has not been determined what role the presence of high dopant concentrations plays in altering quantum transport. For this purpose, we investigated the temperature-dependence of the WAL effect in p-type GeSn (8%) thin film alloys to provide insight into the effect of the presence of high dopant concentrations on the phase and spin coherence. Here, we present measurements of magnetotransport in a series of GeSn alloys with 2D carrier densities of 2.09×10^{12} (low density), 3.65×10^{12} (mid density), and 6.37×10^{12} cm^{-12} (high density), modulated through altering dopant concentrations. From these measurements, the phase coherence lengths (l_{φ}) and upper bounds on the spin–orbit lengths (l_{so}) were extracted using the 2D Hikami–Larkin–Nagaoka (HLN) conductivity correction model with least-squares analysis. The relationships between the extracted phase coherence lengths and calculated decoherence rates are discussed in view of underlying inelastic scattering mechanisms, and it is proposed that inelastic scattering from two-level systems and non-magnetic impurity energy states contribute to phase decoherence behaviors in these GeSn alloys.

II. EXPERIMENTAL

A. Material growth

Germanium tin (GeSn) thin films within nominal compositions of 8% were grown on 500 nm intrinsic germanium buffer layers on Si (100) substrates using chemical vapor deposition (CVD) [Fig. 1(a)]. The material precursors were digermane (Ge_2H_6) and tin tetrachloride ($SnCl_6$). These films were doped with boron during growth to produce "low-," "mid-," and "high"-density samples with nominally 8% Sn. Additional details have been published elsewhere.[23]

B. Material characterization

The composition and strain of the GeSn thin films were characterized by measuring asymmetric (224) reciprocal space maps. It was found that the relaxation of the Ge buffer layer was 105% relative to the Si substrate, while the GeSn layer was coherently strained to the Ge buffer [Fig. 1(b), Fig. S1 in the supplementary material]. The RSM measurements were used to obtain the in-plane and out-of-plane lattice constants for the three samples, which were then used to calculate the effective lattice constants for the GeSn films (Table S1 in the supplementary material). Based on these values, it was found that the Sn composition varied between 8.27% and 8.89% across the three samples [Table I(a)] (see the supplementary material for additional characterization information).

Time-of-flight secondary ion mass spectroscopy (ToF-SIMS) analyses were performed to quantify constituent elements Si, Ge,

Version of Record at:
https://doi.org/10.1063/5.0233728

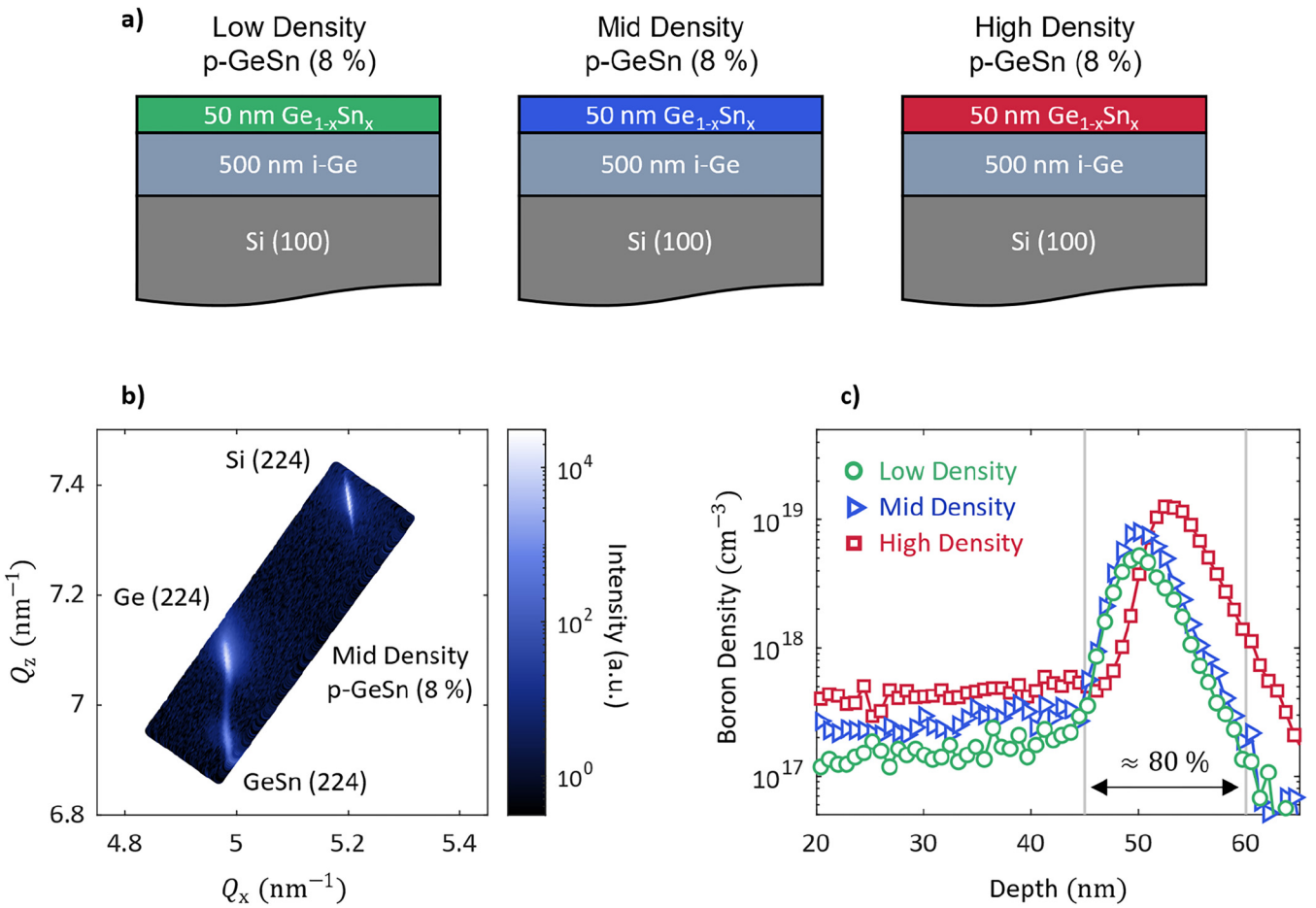

FIG. 1. (a) A series of 50 nm boron-doped GeSn thin film alloys were grown via MOCVD on 500 nm i-Ge buffers on Si (100) substrates. (b) Characterization of the crystal lattice was performed using x-ray diffraction methods, including reciprocal space mapping (RSM). (c) SIMS depth analysis profiles confirm that 80% of the boron is confined to a $9-12$ nm region in the growth axis above the Ge buffer in all three samples. From the depth profiles, 2D boron concentrations of 3.63×10^{12}, 5.61×10^{12}, and 9.44×10^{12} cm^{-2} were quantified.

and Sn in addition to impurities C, and O which confirmed that low concentrations of impurities are present in these materials (Fig. S2 in the supplementary material). Based on the ToF-SIMS, the Sn composition for the three samples ranged between 8.32% and 9.02%, agreeing well with those obtained using XRD-RSM [Table I(b)].

SIMS analyses of the GeSn samples were used to investigate the boron concentrations and depth profiles of boron and Sn relative to Ge (Fig. S3 in the supplementary material). The first 10 nm of the depth profiles were excluded from this analysis to avoid surface artifacts. The depth profiles show that about 80% of boron in each sample is found in a $9-12$ nm region in the

TABLE I. Compositions of the series of GeSn films were estimated from (a) x-ray diffraction methods and measured by (b) ToF-SIMS. (c) SIMS measurements were also performed to obtain depth profiles of boron, which were integrated to obtain 2D densities.

Sample	% Sn–XRD + RSM (a)	% Sn–ToF-SIMS (b)	2D boron density ($\times 10^{12}$ cm^{-2}) (c)
Low density	8.89	8.88	3.63
Mid density	9.09	9.02	5.61
High density	8.27	8.32	9.44

Version of Record at:
https://doi.org/10.1063/5.0233728

growth axis adjacent to the GeSn–Ge interface [Fig. 1(c)]. Total 2D boron concentrations were found to be 3.63×10^{12}, 5.61×10^{12}, and 9.44×10^{12} cm^{-2} for the low-, mid-, and high-density samples [Table I(c)].

The measured SIMS depth profiles were also used to calculate the thicknesses of the GeSn thin films for the three samples (Fig. S3 in the supplementary material). To do this, the magnitude of the Sn signal corresponding to depths between 10 and 40 nm, or within the GeSn film, was averaged for each of the three samples. The differences between these averaged intensities and the lowest measured Sn intensity for each sample were calculated, halved, and subsequently added to the lowest measured intensity, producing estimates of the film thicknesses. The averaged thickness of the three samples is 50 nm $\pm$ 1 nm, in good agreement with the nominal growth thickness.

III. RESULTS AND DISCUSSION

Low-temperature Hall measurements were performed to characterize the carrier densities (p_{2D}), mobilities (μ_p), and sheet resistances ($R_\square$) of the three samples (Fig. 2). The 2D carrier densities were 2.09×10^{12} (low), 3.65×10^{12} (mid), and 6.37×10^{12} cm^{-2} (high) at the base temperature of the dilution refrigerator, indicating carrier freeze out of between 32.5% and 42.4% based on the measured boron concentrations [Fig. 2(a)]. These results indicate that the carrier densities are primarily a function of the dopant concentrations rather than having large contributions from intrinsic carriers. The 2D carrier densities increased with temperature by 30.4%, 24.1%, and 16.0% at 10 K relative to the base temperatures for the low-, mid-, and high-density samples.

The mobilities (μ_p) of the low-, mid-, and high-density samples peaked at 1120, 794, and 653 cm$^2 \cdot$ V$^{-1} \cdot$ s^{-1} at the base temperatures [Fig. 2(b)]. Mobilities increased with decreasing carrier density, and the mobilities of all three samples decreased with increasing temperature by 22.0%, 15.8%, and 9.17% at 10 K relative to the base temperature.

The sheet resistances ($R_\square$) of the samples decreased as a function of increasing carrier densities [Fig. 2(c)]. All three samples had extremely low temperature-dependence, with only a 5.10% decrease in magnitude for the low-density sample and less than 5% decreases for the mid- and high-density samples between the base temperatures and 10 K. This result shows an interesting balance between a positive temperature coefficient of the carrier densities and a negative temperature coefficient of the mobilities of the three samples, which effectively cancel each other out to produce almost constant sheet resistances across this temperature range.

To characterize WAL in the GeSn alloys, their magnetoconductivities were measured in the magnetic field range -5 T to 5 T at temperatures of 30, 100, 300, and 600 mK, and 1.2, 3, 4, 5, 6, 7.5, and 10 K. The magnetoconductivities of the three samples exhibited the WAL effect in a sharp increase in conductivity at a zero magnetic field, $B = 0$ T, which was most prominent at the base temperatures and decreased in magnitude as temperature increased. The datasets were preprocessed by centering the WAL peak at $B = 0$ T, subtracting the zero-field conductivity to produce $\Delta\sigma$, and finally by performing a background subtraction to remove the classical contribution to the magnetoconductivity from the WAL-produced change in

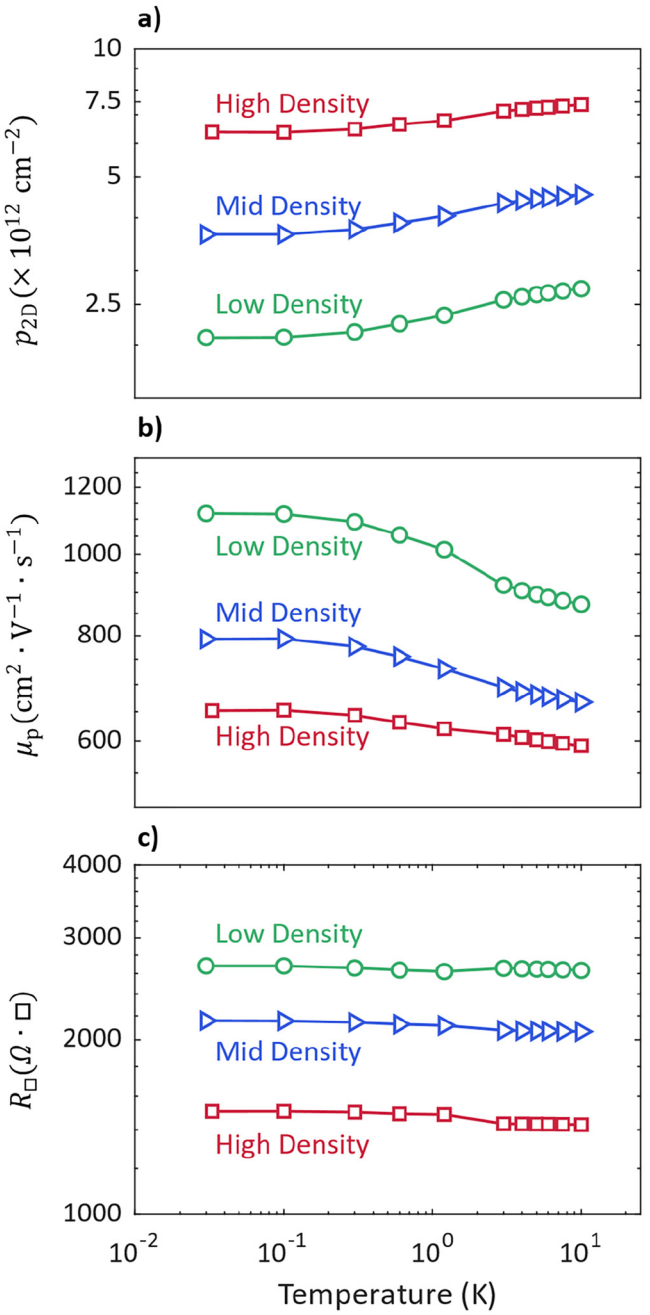

FIG. 2. The temperature-dependence of the (a) 2D carrier density (p_{2D}), (b) mobility (μ_p), and (c) sheet resistance ($R_\square$) of the low-, mid-, and high-density GeSn (8%) samples were obtained using Hall measurements from 30 mK to 10 K.

Version of Record at:
https://doi.org/10.1063/5.0233728

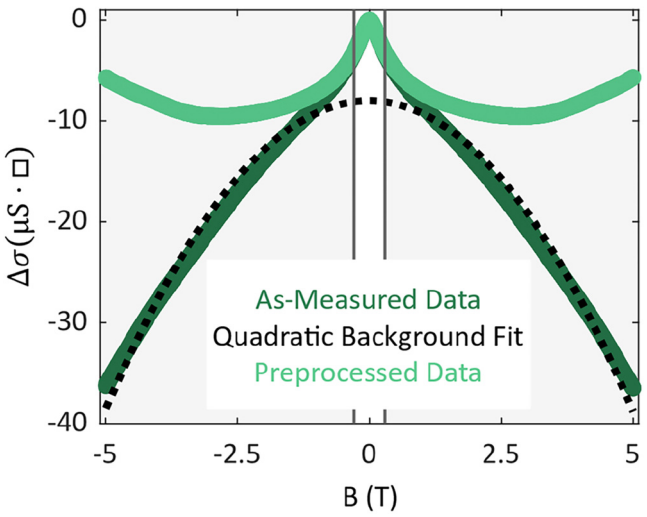

FIG. 3. The magnetoconductivities of the three samples were measured at a series of temperatures—30, 100, 300, and 600 mK, 1.2, 3, 4, 5, 6, 7.5, and 10 K The datasets were preprocessed by centering the WAL peak at $B = 0$ T, subtracting the zero-field conductivity to produce $\Delta\sigma$, and finally subtracting the magnetoconductivity background obtained by fitting the high-field datapoints to a quadratic function. These traces are from the low-density sample at 10 K. Grayed-out regions represent data excluded from the subsequent conductivity correction model fitting.

conductivity ($\sigma_{\text{Classical}} = C_2B^2 + C_1B + C_0$) (Fig. 3). Including a linear term in the background subtraction fitting allows consideration of a linear, odd component to the signal that can be introduced by mixing of R_{xy}. The quadratic background subtraction was applied by fitting the quadratic function to the high field magnetoconductivities in the field ranges of $[-5, -B_{tr}]$ and $[B_{tr}, 5\text{ T}]$, where B_{tr} is the characteristic magnetic field associated with the elastic mean free path of carriers (l_{tr}) according to the equations

$$B_{tr} = \frac{\hbar}{4el_{tr}^2} \tag{1}$$

and

$$l_{tr} = \frac{\mu_p\hbar(2\pi n_{2D})^{\frac{1}{2}}}{e}. \tag{2}$$

Other parameters in these equations include the elementary charge e and the reduced Planck's constant $\hbar$. The estimated l_{tr} varied between 23 and 28 nm for all three samples throughout the range of temperatures.

The perpendicular-field magnetoconductivities of the three samples were fit to the 2D Hikami–Larkin–Nagaoka (HLN) conductivity correction function to extract spin–orbit coupling length scales (Fig. 4).[18] This model is valid for diffusive, 2D carrier systems for which the transport regime is defined such that the mean free path l_{tr} is greater than the film thickness d ($d \ll l_{tr}$), and the dimensionality of the system is defined in terms of the phase coherence length l_φ relative to d for which l_φ is greater than d ($d \ll l_\varphi$).

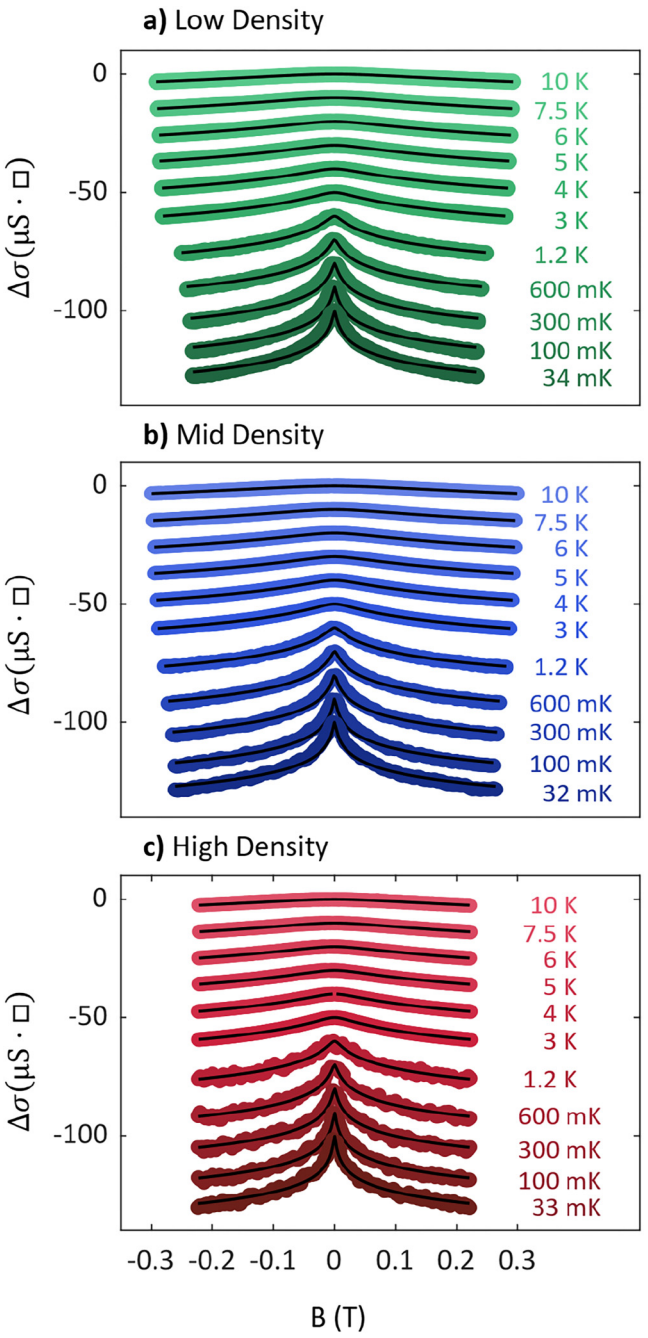

FIG. 4. The processed magnetoconductivities relative to the zero-field magnetoconductivity of the (a) low-, (b) mid-, and (c) high-density samples (offset in increments of 10 μS for clarity). HLN fits are superimposed on the measured data.

Version of Record at:
https://doi.org/10.1063/5.0233728

The HLN function was derived to describe the relationships between carriers and the effective magnetic fields emerging due to their movement in the crystal lattice,[18]

$$\Delta\sigma_{\mathrm{HLN}} = \sigma_{\mathrm{B}} - \sigma_0 = \frac{e^2}{2\pi^2\hbar}\left\{-\frac{1}{2}\psi\left(\frac{1}{2}+\frac{B_\varphi}{B}\right)+\psi\left(\frac{1}{2}+\frac{B_\varphi}{B}+\frac{B_{\mathrm{so}}}{B}\right)+\frac{1}{2}\psi\left(\frac{1}{2}+\frac{B_\varphi}{B}+\frac{2B_{\mathrm{so}}}{B}\right)+\ln\left(\frac{1}{2}+\frac{B_\varphi}{B}\right)-\frac{1}{2}\ln\left(\frac{B_\varphi}{B}+\frac{B_{\mathrm{so}}}{B}\right)-\frac{1}{2}\ln\left(\frac{B_\varphi}{B}+\frac{2B_{\mathrm{so}}}{B}\right)\right\}, \tag{3}$$

where ψ is the digamma function, B is the applied magnetic field, and the effective magnetic fields B_φ and B_{so} relate to the phase coherence length l_φ and the spin–orbit length l_{so} according to

$$B_{\varphi(\mathrm{so})} = \frac{\hbar}{4el^2_{\varphi(\mathrm{so})}}. \tag{4}$$

To fit the magnetoconductivity data, a parametric sweep of $l_{\varphi,\,\mathrm{HLN}}$ $[1-1000\ \mathrm{nm}]$ and $l_{\mathrm{so},\,\mathrm{HLN}}$ $[0.01-100\ \mathrm{nm}]$ was performed using Eq. (3) with least-squares fitting analysis. The magnetoconductivity values used in the fitting corresponded to those in the magnetic field range of $[-B_{\mathrm{tr}},\ B_{\mathrm{tr}}]$, resulting in a temperature- and sample-dependent fitting range. The HLN fits are shown over the measured data in Fig. 4. For $l_{\varphi,\,\mathrm{HLN}}$, 95% confidence intervals were obtained by holding l_{so} constant and computing the covariance matrix for the data. These intervals had a magnitude of around 25 nm at the base temperatures, and rapidly decreased to less than 1 nm at 10 K for each sample set.

To investigate transport dimensionality, temperature-dependent magnetoconductivities were measured for the high-density alloy under a parallel B field at temperatures of ≅30, 100, 300, and 600 mK, 1.2, 3, 4, 5, 6, 7.5, and 10 K in the magnetic field range from −5 T to 5 T (Fig. 5). The sample was found to be oriented $1^\circ \pm 3^\circ$ from parallel relative to the direction of current flow based on the slope of a linear fit of the magnetic field and Hall resistances. Comparing the parallel-field magnetoconductivities to the perpendicular-field data, a contrast is seen in the relative magnitudes and width of the WAL conductivity correction $\Delta\sigma$ at each temperature [Fig. 5(a)]. The magnetoconductivity peaks are broader and lower in relative magnitude in the parallel-field magnetoconductivities relative to the perpendicular-field magnetoconductivities. A change is also seen in the high-field data, for which the perpendicular orientation has a parabolic background while the background for the parallel-field data is flatter.

The parallel-field magnetoconductivities were fit to the Dugaev–Khmel'nitskii (DK) conductivity model for 2D transport in a parallel magnetic field in the limit that the film thickness is less than the mean free path ($d \ll l_{\mathrm{tr}}$),[25]

$$\Delta\sigma_{\mathrm{DK}} = \sigma_{B,\|} - \sigma_{0,\|} = -N\frac{e^2}{4\pi^2\hbar}\ln\left(1+\frac{B_\|}{B_\varphi}\right). \tag{5}$$

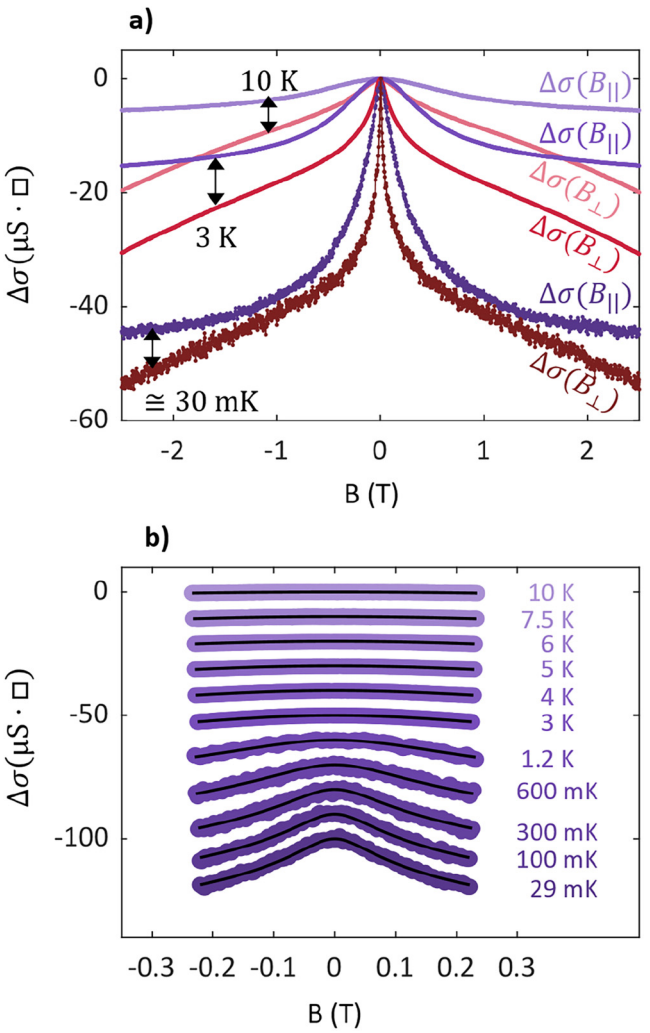

FIG. 5. The magnetoconductivity of the high-density sample was measured at a series of temperatures—30, 100, 300, and 600 mK, and 1.2, 3, 4, 5, 6, 7.5, and 10 K—to confirm the 2D transport dimensionality. (a) Comparison of magnetoconductivities relative to the zero-field values ($\Delta\sigma = \sigma_B - \sigma_0$) of the high-density alloy for perpendicular- and parallel-magnetic field orientations at temperatures ≅30 mK, 3 K, and 10 K. (b) Parallel-field magnetoconductivities for all temperatures were fit to the Dugaev–Khmel'Nitskii (DK) conductivity correction model.[25]

In this model, the conductivity correction is a function of the thin film thickness d through the expression

$$B_\| = \frac{eB^2}{4\hbar d}\left(\frac{\hbar}{4eB_{\mathrm{tr}}}\right)^{\frac{1}{2}}. \tag{6}$$

The film thickness of 50 nm is larger than the mean free paths across the temperature range ($26\ \mathrm{nm} < l_{\mathrm{tr}} < 28\ \mathrm{nm}$ for the high-density alloy). Based on the SIMS data (Fig. 1) which showed that

Version of Record at:
https://doi.org/10.1063/5.0233728

the boron concentration is highest at the interface, we assumed a relative confinement of the majority of the carriers within the ≅10 nm region above the interface and used a thickness parameter $d = 10$ nm to fit the data, consequently meeting the relative length scale criterion for the DK model. The data were preprocessed and fit to Eq. (5) using the same procedure as the HLN conductivity correction fitting with only one fitting parameter—l_φ. The closeness of the model fits to the data indicates a good theoretical fit for 2D transport, with least-squares values of the parametric fit parameter closely matching those obtained using the HLN model with the parallel-field data. While validating that 2D transport occurs throughout this temperature range, these findings also substantiate majority carrier confinement to a region that is narrower than the film thickness.

In the low-density sample, $l_{\varphi,\,\mathrm{HLN}}$ decreased from 577 nm at the base temperature to 62 nm at 10 K [Fig. 6(a)]. Similarly, $l_{\varphi,\,\mathrm{HLN}}$

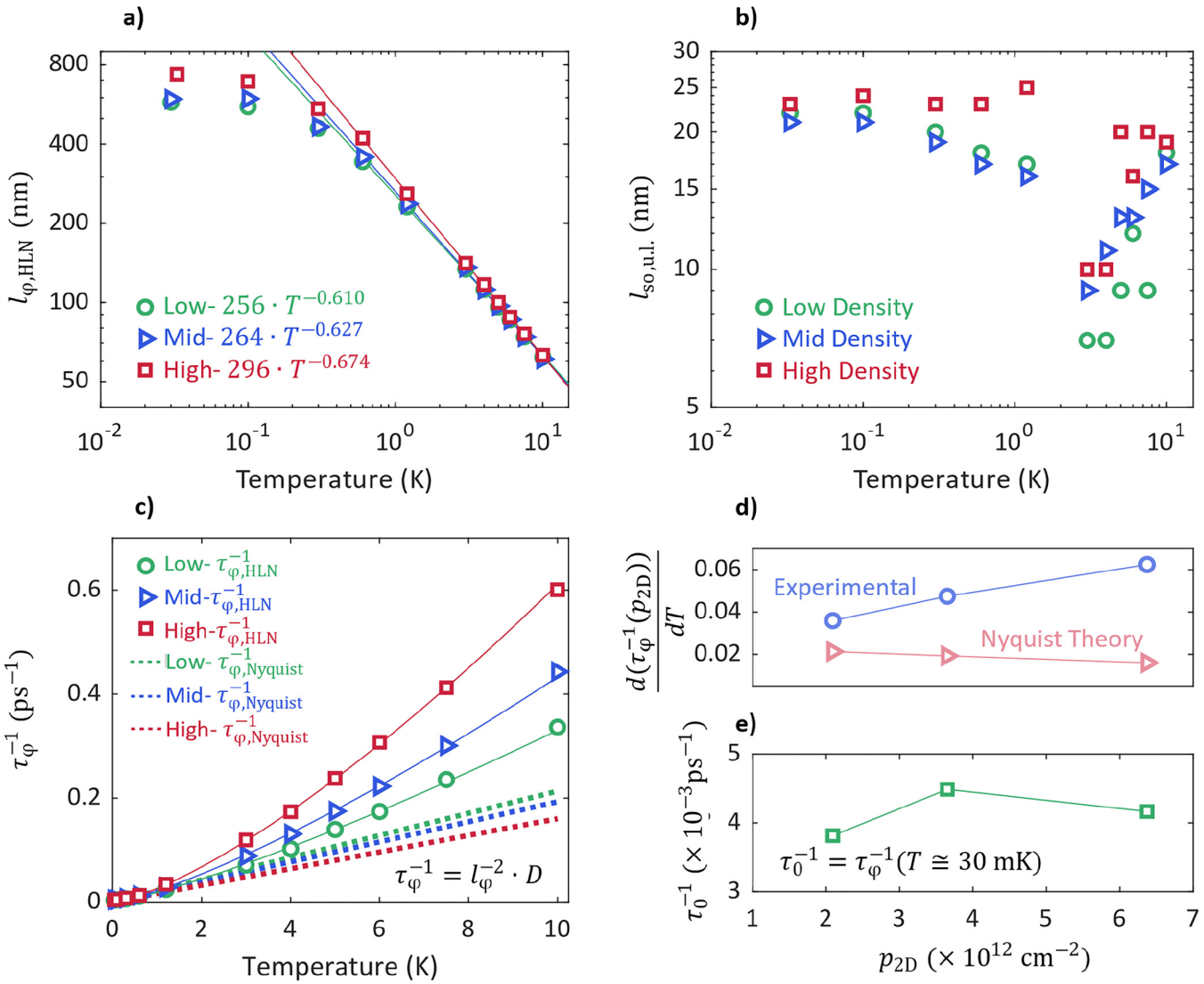

FIG. 6. The (a) phase coherence lengths ($l_{\varphi,\,\mathrm{HLN}}$) and (b) estimates on the upper limits of the spin–orbit lengths ($l_{\mathrm{so,\,u.\,l.}}$) for the three samples were extracted from the measured magnetoconductivities by parametrically fitting that data to the 2D Hikami–Larkin–Nagaoka conductivity correction function. (c) The experimental (τ^{-1}_{HLN}) and theoretical ($\tau^{-1}_{\mathrm{Nyquist}}$) phase decoherence rates were calculated from the phase coherence lengths and calculated diffusivities of the three samples. (d) Finally, the rate of change of the phase decoherence rate with respect to temperature $\left(\frac{d\tau_\varphi^{-1}}{dT}\right)$ and the (e) base phase decoherence rates (τ_0^{-1}) were calculated from the phase decoherence rates for each sample. Lines on (d) and (e) are guides to the eye.

Version of Record at:
https://doi.org/10.1063/5.0233728

TABLE II. A summary of the electronic parameters extracted from the (a) low-, (b) mid-, and (c) high-density p-GeSn (8%) samples. Values correspond to the base temperatures of ≅30 mK where relevant.

	(a) Low density	(b) Mid density	(c) High density
p_{2D} ($\times 10^{12}$ cm^{-2})	2.09	3.65	6.37
μ_p (cm$^2 \cdot$ V$^{-1} \cdot$ s^{-1})	1120	794	653
$R_\square$ ($\Omega \cdot \square$)	2680	2160	1500
$l_{\varphi,\ \mathrm{HLN}}$ (nm)	577	593	737
$l_{\mathrm{so,\ u.l.}}$ (nm)	22	21	23
N (no. subbands)	1	1	1
m^*/m_0	0.436	0.436	0.436
D (cm$^2 \cdot$ s^{-1})	12.7	15.8	22.6
$\frac{d\tau_\varphi^{-1}}{dT}$ (ps$^{-1} \cdot$ K^{-1})	0.0360	0.0475	0.0625
τ_0^{-1} (ps^{-1})	3.81×10^{-3}	4.49×10^{-3}	4.17×10^{-3}

decreased from 593(737) nm to 61(63) nm for the mid(high)-density sample. The phase coherence lengths were greater than the mean free paths [Eq. (2)], indicating a diffusive system and validating the use of the 2D HLN model for analysis.[26]

Due to the minimal least-squares error occurring over a wide range of l_{so} values, we can only provide an estimate of an upper limit on $l_{\mathrm{so,\ HLN}} - l_{\mathrm{so,\ u.l.}}$ [Fig. 6(b)] (see the supplementary material). The digamma function loses sensitivity to input changes as the input value increases, corresponding in our analyses to decreasing lengths [Eqs. (3) and (4)] (Fig. S4 in the supplementary material).[27] Based on the parametric values producing least-squares error within 5% of the magnitude of the minima of our parametric searches, we believe that l_{so} is less than 25 nm in all three samples across all temperatures [Fig. 6(b)]. This estimated upper limit demonstrates that strong spin–orbit coupling is present in these materials, in which the hole spins rotate over shorter distances than the estimated elastic mean free paths. There is minimal temperature-dependence and carrier-density dependence in l_{so} due to its relationship with the effective magnetic fields from the crystalline lattice.

The phase coherence lengths followed power-law temperature-dependences for temperatures $T > T_{sat}$ where the saturation temperature is 300 mK $< T_{sat} <$ 600 mK. The power values ($p = -0.610, -0.627, -0.674$ for the low-, mid-, and high-density samples) deviate from but are close to the power $p = 0.5$ predicted for the phase coherence lengths of 2D systems by the Nyquist equation for inelastic carrier scattering,[22]

$$l_{\varphi,\ \mathrm{Nyquist}} = \left(\frac{2\pi\hbar^2 D}{e^2 k_B R_\square} \frac{1}{\ln\left(\frac{\pi\hbar}{e^2 R_\square}\right)} \right)^{\frac{1}{2}} T^{-\frac{1}{2}}. \quad (7)$$

The pre-factor to the temperature-dependence is a function of the carrier density and mobility of the material through the sheet resistance $R_\square$ and the diffusivity D,

$$D = \frac{1}{N} \frac{\pi\hbar^2}{e m^*} \mu_p p_{2D}, \quad (8)$$

where the effective mass m^* and the number of occupied subbands N were estimated based on 1D Schrödinger–Poisson calculations (Table II).[28] This pre-factor is typically estimated as a constant for small ranges of temperatures.[12,22] As written, this form of the Nyquist model predicts the temperature-dependence of the phase coherence length based solely on carrier–carrier scattering and consequently deviations from it are likely due to the presence of additional inelastic scattering mechanisms contributing to phase decoherence, such as temperature-dependent contributions from electron–phonon scattering or temperature-independent contributions from other inelastic scattering mechanisms. While the Nyquist model is generally considered to reliably predict transport dimensionality, deviations from this theory have been reported.[26,29] We note that while we cannot rule out the variability in composition contributing to some degree to phase coherence in our samples, this variability would be incorporated into this model through the diffusivity and sheet resistance terms in the pre-factor.

The Nyquist model predicts that $l_{\varphi,\ \mathrm{Nyquist}}$ increases with increasing carrier density through its pre-factor [Eq. (7)].[12,30] However, very minimal carrier-density dependences of $l_{\varphi,\ \mathrm{HLN}}$ were calculated from fitting magnetoconductivities, despite the range of densities measured across the sample set (Table II). To further probe the carrier-density dependence of the dephasing mechanism, the phase decoherence rates were calculated from $l_{\varphi,\ \mathrm{HLN}}$ using the equation

$$\tau_\varphi^{-1} = l_\varphi^{-2} D. \quad (9)$$

Theoretical Nyquist decoherence lengths ($l_{\varphi,\ \mathrm{Nyquist}}$) were also calculated using Eq. (7) from the measured transport properties and estimated diffusivities, and they were subsequently used to calculate the theoretical phase decoherence rates using Eq. (9) [Fig. 6(c)].

While phase decoherence rates are predicted to increase linearly with temperature, the measured temperature-dependences of our samples are superlinear [Fig. 6(c)]. Additionally, while the Nyquist model predicts decreasing phase decoherence rates with increasing carrier density, the opposite is found in the experimental results. This point is more clearly illustrated in observing the trends of the experimental vs theoretical changes in the decoherence rates with respect to changes in temperature, which were obtained for

Version of Record at:
https://doi.org/10.1063/5.0233728

the experimental values by linearly fitting $\tau_{\varphi,\mathrm{HLN}}^{-1}$ corresponding to temperatures at and above 600 mK [Fig. 6(d)].

In addition to predicting a strong dependence of τ_{φ}^{-1} on carrier density, the Nyquist model predicts that $\tau_{\varphi,\mathrm{Nyquist}}^{-1} \to 0$ as $T \to 0$ K. We do not observe this behavior in $\tau_{\varphi,\mathrm{HLN}}^{-1}$, in disagreement with our observation of a nonzero temperature-independent base scattering rate τ_0^{-1} based on the asymptotic behavior at the lowest temperatures [Fig. 6(e)].

The Nyquist model imperfectly fits our data due to the low carrier-density dependence of the phase decoherence behaviors and the presence of a base scattering rate as $T \to 0$ K. As the experimentally obtained decoherence rates are overall larger than the Nyquist rates, between 37% and 227% at 10 K, it is likely that additional phase decoherence mechanisms are present in addition to Nyquist temperature-dependent inelastic carrier scattering, contributing significantly to dephasing electron waves in these alloys.

While little to no carrier-density dependence was seen for phase coherence lengths at higher temperatures, their values increased with carrier density at the base temperature [Fig. 6(a)]. Temperature-dependent saturation of phase coherence lengths at low temperatures has been shown previously in a variety of different material systems.[31–40] It is frequently attributed to an external factor, such as microwave irradiation or Joule heating, that prevents the electrons from cooling down below some saturation temperature.[41–44] Measurements were also performed using three orders-of-magnitude different applied currents to ensure that the current used at each temperature was not noticeably causing a Joule heating effect (Fig. S5 in the supplementary material). While these results point toward an intrinsic rather than extrinsic source for phase decoherence in these samples, we cannot quantify other factors that may cause the electron temperatures to saturate and therefore we cannot definitively rule out a heating-related cause for temperature saturation.

Intrinsic causes for temperature saturation explored in other studies include the crossover between transport dimensions and temperature-independent magnetic scattering.[27,34,45–50] Dimensional crossover occurs when the phase coherence lengths are large relative to some dimension of the sample under investigation. As it was confirmed that transport was 2D across the experiments' temperatures, and based on our microscale device dimensions, we do not believe that dimensional crossover produced the temperature saturation in our samples. Additionally, due to the high purity of the precursors used to grow our materials, it is unlikely that magnetic scattering due to unintentional dopants is the underlying cause of saturation.[51]

Intrinsic saturation of the phase coherence lengths in these GeSn thin films could be caused by the presence of point defects with close energy states, called two-level systems (TLSs) or dynamical defects.[52–54] TLSs are often associated with scattering at interfaces, surfaces, or dislocations. They scatter inelastically with carriers to switch between degenerate energy states separated by small energy barriers, thereby resulting in a temperature-independent source for phase decoherence.[55–57] We also note that high boron concentrations are present in close proximity to the 2D holes in our samples (see Fig. 1). The acceptor states associated with boron dopants and their clusters could introduce many effective TLS and possibly impurity bands, exchanging carriers and energy among themselves and with the 2D hole system and resulting in an additional inelastic scattering mechanism.

Based on our results, it is likely that inelastic scattering mechanisms that are intrinsically tied to localized defects and nonmagnetic impurities are an influential factor in the phase decoherence behaviors of GeSn alloys. These intrinsic sources of dephasing, which self-limit the magnitudes of phase coherence lengths at low temperatures, are intriguing directions for further investigations into group-IV alloys. The possibility of multiple intrinsic dephasing sources indicates a need to ascertain the distinct roles of interfacial defects and impurity densities in inelastic scattering.

Figure 7 displays the ranges of coherence lengths found in the literature in group-IV materials—Si, SiGe, Ge, and GeSn—as a function of carrier density, illustrating a nuanced relationship between the two parameters. This snapshot of published values corresponds to ungated and gated WL and WAL measurements of materials with carrier densities ranging from 1.3×10^{11} to 1.4×10^{15} cm^{-2}, at temperatures between 260 mK and 2.2 K, and measured coherence lengths from 42 nm to 3.3 μm. Our coherence lengths for our low-, mid-, and high-density GeSn (8%) samples, measured at the base temperatures, are overlaid on the literature values.

In undoped materials, coherence lengths increased with increasing carrier density for all datasets. In the doped materials, control over carrier densities was obtained by using different dopant concentrations, as was demonstrated with our measurements. These studies found that increasing the carrier density increased their measured l_{φ}, and generally found that the n-doped materials had slightly shorter l_{φ} than p-doped materials.[12,24]

Other studies focused on holding carrier densities approximately constant to study the effect of other parameters, such as

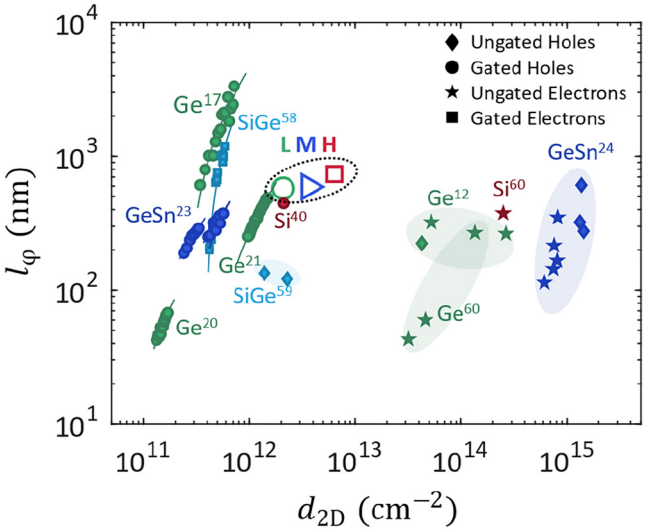

FIG. 7. A selection of phase coherence lengths (l_{φ}) of group-IV materials is presented as a function of carrier density (d_{2D}), at the lowest recorded temperatures from each publication (260 mK – 2.3 K). Our data correspond to the base temperatures of 30 mK for the low-, mid-, and high-density alloys. The data shown in this figure are compiled from digitized datasets.[12,17,20,21,23,24,40,58–60]

Version of Record at:
https://doi.org/10.1063/5.0233728

composition, which also played an important role in the phase decoherence behavior. For instance, it was found that l_φ decreased as Sn content increased in a study of GeSn (1%–8%).[24]

Our research adds to the current understanding of both quantum transport behaviors in GeSn alloys and more generally of modulation of electronic structure using impurity densities in group-IV alloys, providing information regarding the temperature-dependence and carrier-density-dependence of phase decoherence mechanisms in moderately doped GeSn (8%) alloys. While direct comparisons with literature values are difficult given the variability in the compositions and structures of the samples investigated previously, our measured phase coherence lengths are on the same order as many of other experiments, even relative to those of some high mobility heterostructures. Our findings highlight the potential of GeSn materials and devices to perform favorably relative to other group-IV materials.

IV. SUMMARY AND CONCLUSIONS

In this work, the weak antilocalization effect was measured in a series of p-GeSn (8%) alloys to determine the role of changing dopant densities on their temperature-dependent phase decoherence mechanisms. The magnetoconductivities of these alloys were measured at temperatures between 30 mK to 10 K and were subsequently fit to the 2D Hikami–Larkin–Nagaoka conductivity correction model to extract spin–orbit coupling lengthscales: the phase coherence length l_φ and the spin–orbit length l_{so}. Maximum phase coherence length values of 577, 593, and 737 nm were obtained at the base temperatures for the low-, mid-, and high-density samples. The phase coherence lengths were found to follow power-law temperature-dependences at higher temperatures at and above 600 mK, below which the coherence lengths saturated. Upper estimates of l_{so} were less than 25 nm across all samples and temperatures, demonstrating strong spin–orbit coupling.

Phase decoherence rates ($\tau^{-1}_{\varphi,\mathrm{HLN}}$) were calculated from the $l_{\varphi,\mathrm{HLN}}$ values and compared to theoretical values predicted by the Nyquist model ($\tau^{-1}_{\varphi,\mathrm{Nyquist}}$) for inelastic carrier scattering, which predicts strong temperature and carrier-density dependences of phase decoherence in 2D systems. It was found that the temperature-dependences of the high-temperature data were comparable to those predicted by the Nyquist model. However, temperature-dependent behavior of the phase decoherence rates and their low dependence on carrier density indicated a poor model fit. In light of these results and the temperature saturation of phase coherence, it was proposed that additional intrinsic inelastic scattering mechanisms were present in the materials, such as two-level systems or impurity band scattering. Future studies include identifying the underlying mechanisms contributing to phase decoherence. This work is an important step toward understanding quantum transport behaviors of GeSn alloys.

V. METHODS

A. Lithography

To characterize transport and spin–orbit coupling in the GeSn thin films, six-contact Hall bar devices ($W = 40$ μm, $L = 200$ μm) were fabricated using standard cleanroom processes.

B. Transport

To quantify spin–orbit coupling in the GeSn samples, a ^{3}He/^{4}He dilution refrigerator was used to measure low-temperature magnetoconductivity in the three samples. To perform these measurements, standard lock-in procedures were used to measure the current through the device and the longitudinal (V_{xx}) and Hall (V_{xy}) voltages as a function of magnetic field and temperature of five-terminal device configurations for the samples. The electrical current used to perform these measurements was 1 nA at $T > 1.2$ K, and 100 nA at $T \leq 1.2$ K to ensure that the WAL effect was not dampened by Joule heating in the device. The magnetic field was swept between −5 and 5 T at a rate of 0.05 T · min^{-1}. The magnetic field was calibrated using an InAs Hall sensor. Temperatures included a base temperature around 30 mK which varied slightly depending on the condensation cycle, as well as 100, 300, and 600 mK, 1.2, 3, 4, 5, 6, 7.5, and 10 K. Lines into the dilution refrigerator were filtered using multi-stage low-pass filters (QFilters by QDevil) designed for low noise and low electron temperatures for quantum devices. These datasets were also used to calculate transport properties at those temperature values.

SUPPLEMENTARY MATERIAL

See the supplementary material for additional information and figures regarding the material characterization and validation of the electrical experiments.

ACKNOWLEDGMENTS

This work was supported as part of μ-ATOMS, an Energy Frontier Research Center funded by the U.S. Department of Energy, Office of Science, Basic Energy Sciences under Award No. DE-SC0023412. This work was performed, in part, at the Center for Integrated Nanotechnologies, an Office of Science User Facility operated for the U.S. Department of Energy (DOE) Office of Science. Sandia National Laboratories is a multimission laboratory managed and operated by National Technology & Engineering Solutions of Sandia, LLC, a wholly owned subsidiary of Honeywell International, Inc., for the U.S. DOE's National Nuclear Security Administration under Contract No. DE-NA-0003525. This article has been authored by an employee of National Technology & Engineering Solutions of Sandia, LLC under Contract No. DE-NA0003525 with the U.S. Department of Energy (DOE). The employee owns all right, title and interest in and to the article and is solely responsible for its contents. The United States Government retains and the publisher, by accepting the article for publication, acknowledges that the United States Government retains a non-exclusive, paid-up, irrevocable, world-wide license to publish or reproduce the published form of this article or allow others to do so, for United States Government purposes. The DOE will provide public access to these results of federally sponsored research in accordance with the DOE Public Access Plan (https://www.energy.gov/downloads/doe-public-access-plan). This paper describes objective technical results and analysis. Any subjective views or opinions that might be expressed in the paper do not necessarily represent the views of the U.S. Department of Energy or the United States Government. S. D. acknowledges the MonArk

Version of Record at:
https://doi.org/10.1063/5.0233728

NSF Quantum Foundry supported by the National Science Foundation Q-AMASE-i program under National Science Foundation Award No. DMR-1906383. H.Z. and Y.Z. acknowledge National Science Foundation Award No. 2328840. The authors would like to thank Professor Jin Hu at the University of Arkansas for his helpful discussions on the quantum transport behaviors presented in this work.

AUTHOR DECLARATIONS

Conflict of Interest

The authors have no conflicts to disclose.

Author Contributions

Adelaide Bradicich: Formal analysis (lead); Investigation (lead); Validation (supporting); Visualization (lead); Writing – original draft (lead); Writing – review & editing (supporting). **Priyanka Petluru:** Investigation (supporting); Writing – review & editing (supporting). **Shiva Davari:** Validation (lead). **Haochen Zhao:** Investigation (supporting); Writing – review & editing (supporting). **Siddhant Gangwal:** Investigation (supporting). **Chia-You Liu:** Resources (equal). **Dragica Vasileska:** Investigation (supporting). **Yuping Zeng:** Investigation (supporting). **Hugh Churchill:** Validation (supporting); Writing – review & editing (supporting). **Jiun-Yun Li:** Resources (equal). **Michael P. Lilly:** Conceptualization (supporting); Formal analysis (supporting); Investigation (supporting); Supervision (lead); Writing – review & editing (supporting). **Tzu-Ming Lu:** Conceptualization (lead); Formal analysis (supporting); Funding acquisition (lead); Investigation (supporting); Supervision (supporting); Writing – review & editing (supporting).

DATA AVAILABILITY

The data that support the findings of this study are available from the corresponding author upon reasonable request.

REFERENCES

[1]J. Zheng *et al.*, "Recent progress in GeSn growth and GeSn-based photonic devices*," J Semicond. **39**, 061006 (2018).
[2]O. Olorunsola *et al.*, "SiGeSn quantum well for photonics integrated circuits on Si photonics platform: A review," J. Phys. D: Appl. Phys. **55**, 443001 (2022).
[3]V. D'Costa, J. Kouvetakis, J. Menendez, R. Soref, and J. Tolle, "Advances in SiGeSn technology," J. Mater. Res. **22**, 3281–3291 (2007).
[4]S. Wirths, D. Buca, and S. Mantl, "Si–Ge–Sn alloys: From growth to applications," Prog. Cryst. Growth Charact. Mater. **62**, 1–39 (2016).
[5]V. R. D'Costa *et al.*, "Optical critical points of thin-film $Ge_{1-y}Sn_y$ alloys: A comparative $Ge_{1-y}Sn_y/Ge_{1-x}Si_x$ study," Phys. Rev. B **73**, 125207 (2006).
[6]R. A. Soref and C. H. Perry, "Predicted band gap of the new semiconductor SiGeSn," J. Appl. Phys. **69**, 539–541 (1991).
[7]H. Pérez Ladrón de Guevara, A. G. Rodríguez, H. Navarro-Contreras, and M. A. Vidal, "Nonlinear behavior of the energy gap in $Ge_{1-x}Sn_x$ alloys at 4 K," Appl. Phys. Lett. **91**, 161909 (2007).
[8]R. W. Olesinski and G. J. Abbaschian, "The Ge–Sn (germanium–tin) system," Bull. Alloy Phase Diagrams **5**, 265–271 (1984).
[9]S. Wirths *et al.*, "Lasing in direct-bandgap GeSn alloy grown on Si," Nat. Photonics **9**, 88–92 (2015).
[10]S. A. Ghetmiri *et al.*, "Direct-bandgap GeSn grown on silicon with 2230 nm photoluminescence," Appl. Phys. Lett. **105**, 151109 (2014).
[11]J. Foronda, C. Morrison, J. E. Halpin, S. D. Rhead, and M. Myronov, "Weak antilocalization of high mobility holes in a strained germanium quantum well heterostructure," J. Phys.: Condens. Matter **27**, 022201 (2015).
[12]P. J. Newton, R. Mansell, S. N. Holmes, M. Myronov, and C. H. W. Barnes, "Weak localization and weak antilocalization in doped germanium epilayers," Appl. Phys. Lett. **110**, 062101 (2017).
[13]A. Marchionni *et al.*, "Inverse spin-Hall effect in GeSn," Appl. Phys. Lett. **118**, 212402 (2021).
[14]K. Wang *et al.*, "Ultrafast coherent control of a hole spin qubit in a germanium quantum dot," Nat. Commun. **13**, 206 (2022).
[15]J.-C. Rojas-Sánchez *et al.*, "Spin pumping and inverse spin Hall effect in germanium," Phys. Rev. B **88**, 064403 (2013).
[16]M. M. Glazov and L. E. Golub, "Nondiffusive weak localization in two-dimensional systems with spin-orbit splitting of the spectrum," Semiconductors **40**, 1209–1217 (2006).
[17]C.-T. Chou *et al.*, "Weak anti-localization of two-dimensional holes in germanium beyond the diffusive regime," Nanoscale **10**, 20559–20564 (2018).
[18]S. Hikami, A. I. Larkin, and Y. Nagaoka, "Spin-orbit interaction and magnetoresistance in the two dimensional random system," Prog. Theor. Phys. **63**, 707–710 (1980).
[19]S. V. Iordanskii, Y. B. Lyanda-Geller, and G. E. Pikus, "Weak localization in quantum wells with spin-orbit interaction," ZhETF Pisma Redaktsiiu **60**, 199 (1994).
[20]R. Mizokuchi *et al.*, "Hole weak anti-localization in a strained-Ge surface quantum well," Appl. Phys. Lett. **111**, 063102 (2017).
[21]R. Moriya *et al.*, "Cubic Rashba spin-orbit interaction of a two-dimensional hole gas in a strained-Ge/SiGe quantum well," Phys. Rev. Lett. **113**, 086601 (2014).
[22]B. L. Altshuler, A. G. Aronov, and D. E. Khmelnitsky, "Effects of electron-electron collisions with small energy transfers on quantum localisation," J. Phys. C **15**, 7367 (1982).
[23]C.-T. Tai *et al.*, "Strain effects on Rrashba spin-orbit coupling of 2D hole gases in GeSn/Ge heterostructures," Adv. Mater. **33**, 2007862 (2021).
[24]D. Weißhaupt *et al.*, "Weak localization and weak antilocalization in doped $Ge_{1-y}Sn_y$ layers with up to 8% Sn," J. Phys.: Condens. Matter **33**, 085703 (2021).
[25]V. K. Dugaev and D. E. Khmel'Nitskii, "Magnetoresistance of metal films with low impurity concentrations in a parallel magnetic field," Zh. Eksp. Teor. Fiz **86**, 1784–1790 (1984).
[26]D. E. Beutler and N. Giordano, "Localization and electron-electron interaction effects in thin Bi wires and films," Phys. Rev. B **38**, 8–19 (1988).
[27]J. J. Lin and N. Giordano, "Localization and electron-electron interaction effects in thin Au-Pd films and wires," Phys. Rev. B **35**, 545–556 (1987).
[28]S. Gangwal, S. Chen, T. Li, T.-M. Lu, and D. Vasileska, "Modeling and simulation of electrostatics of $Ge_{1-x}Sn_x$ layers grown on Ge substrates," IEEE J. Select. Topics Quant. Electron. **31**(1), 7900108 (2024).
[29]D. Natelson, R. L. Willett, K. W. West, and L. N. Pfeiffer, "Geometry-dependent dephasing in small metallic wires," Phys. Rev. Lett. **86**, 1821–1824 (2001).
[30]E. M. Likovich, K. J. Russell, E. W. Petersen, and V. Narayanamurti, "Weak localization and mobility in ZnO nanostructures," Phys. Rev. B **80**, 245318 (2009).
[31]R. M. Mueller, R. Stasch, and G. Bergmann, "Anomalous T12 law of the dephasing rate in Au films down to 20 mK," Solid State Commun. **91**, 255–258 (1994).
[32]A. B. Gougam, F. Pierre, H. Pothier, D. Esteve, and N. O. Birge, "Comparison of energy and phase relaxation in metallic wires," J. Low Temp. Phys. **118**, 447–456 (2000).
[33]S. Islam *et al.*, "Low-temperature saturation of phase coherence length in topological insulators," Phys. Rev. B **99**, 245407 (2019).
[34]P. Fournier *et al.*, "Anomalous saturation of the phase coherence length in underdoped $Pr_{2-x}Ce_xCuO_4$ thin films," Phys. Rev. B **62**, R11993–R11996 (2000).

[35]J. J. Lin and J. P. Bird, "Recent experimental studies of electron dephasing in metal and semiconductor mesoscopic structures," J. Phys.: Condens. Matter **14**, R501 (2002).
[36]Y. A. Salawu, J. H. Yun, J.-S. Rhyee, M. Sasaki, and H.-J. Kim, "Weak antilocalization, spin–orbit interaction, and phase coherence length of a dirac semimetal $Bi_{0.97}Sb_{0.03}$," Sci. Rep. **12**, 2845 (2022).
[37]H. Nakamura *et al.*, "Robust weak antilocalization due to spin-orbital entanglement in Dirac material Sr_3SnO," Nat. Commun. **11**, 1161 (2020).
[38]M. Rudolph and J. J. Heremans, "Spin-orbit interaction and phase coherence in lithographically defined bismuth wires," Phys. Rev. B **83**, 205410 (2011).
[39]J. J. Lin, Y. L. Zhong, and T. J. Li, "Effect of annealing on electron dephasing in three-dimensional polycrystalline metals," Europhys. Lett. **57**, 872 (2002).
[40]D. M. Pooke, N. Paquin, M. Pepper, and A. Gundlach, "Electron-electron scattering in narrow Si accumulation layers," J. Phys.: Condens. Matter **1**, 3289 (1989).
[41]X.-J. Hao *et al.*, "Strong and tunable spin−orbit coupling of one-dimensional holes in Ge/Si core/shell nanowires," Nano Lett. **10**, 2956–2960 (2010).
[42]Y. B. Khavin, M. E. Gershenson, and A. L. Bogdanov, "Decoherence and the thouless crossover in one-dimensional conductors," Phys. Rev. Lett. **81**, 1066–1069 (1998).
[43]F. Pierre and N. O. Birge, "Dephasing by extremely dilute magnetic impurities revealed by Aharonov–Bohm oscillations," Phys. Rev. Lett. **89**, 206804 (2002).
[44]S. A. Vitkalov, G. M. Gusev, Z. D. Kvon, G. I. Leviev, and V. I. Fal'ko, "Dynamic effect of a microwave field on weak localization," Sov. Phys. JETP **67**, 1080 (1988).
[45]M. Noguchi, T. Ikoma, T. Odagiri, H. Sakakibara, and S. N. Wang, "Saturation of electron phase breaking time in GaAs/AlGaAs quantum wires," J. Appl. Phys. **80**, 5138–5144 (1996).
[46]W. Stefanowicz *et al.*, "Experimental determination of Rashba spin-orbit coupling in wurtzite n-GaN:Si," Phys. Rev. B **89**, 205201 (2014).
[47]T. Hiramoto, K. Hirakawa, Y. Iye, and T. Ikoma, "Phase coherence length of electron waves in narrow AlGaAs/GaAs quantum wires fabricated by focused ion beam implantation," Appl. Phys. Lett. **54**, 2103–2105 (1989).
[48]S. A. Studenikin, P. T. Coleridge, N. Ahmed, P. J. Poole, and A. Sachrajda, "Experimental study of weak antilocalization effects in a high-mobility $In_xGa_{1-x}AsInP$ quantum well," Phys. Rev. B **68**, 035317 (2003).
[49]P. Mohanty, E. M. Q. Jariwala, and R. A. Webb, "Intrinsic decoherence in mesoscopic systems," Phys. Rev. Lett. **78**, 3366–3369 (1997).
[50]J. J. Lin and N. Giordano, "Electron scattering times from weak localization studies of Au-Pd films," Phys. Rev. B **35**, 1071–1075 (1987).
[51]F. Pierre *et al.*, "Dephasing of electrons in mesoscopic metal wires," Phys. Rev. B **68**, 085413 (2003).
[52]J. J. Lin, T. J. Li, and Y. L. Zhong, "Electron dephasing near zero temperature: An experimental review," J. Phys. Soc. Jpn. **72**, 7–12 (2003).
[53]C. Müller, J. H. Cole, and J. Lisenfeld, "Towards understanding two-level-systems in amorphous solids: Insights from quantum circuits," Rep. Prog. Phys. **82**, 124501 (2019).
[54]S. Islam, S. Shamim, and A. Ghosh, "Benchmarking noise and dephasing in emerging electrical materials for quantum technologies," Adv. Mater. **35**, 2109671 (2023).
[55]A. Zrenner *et al.*, "Coherent properties of a two-level system based on a quantum-dot photodiode," Nature **418**, 612–614 (2002).
[56]A. Trionfi, S. Lee, and D. Natelson, "Time-dependent universal conductance fluctuations and coherence in AuPd and Ag," Phys. Rev. B **72**, 035407 (2005).
[57]A. Zawadowski, J. von Delft, and D. C. Ralph, "Dephasing in metals by two-level systems in the 2-channel Kondo regime," Phys. Rev. Lett. **83**, 2632–2635 (1999).
[58]S. J. Koester, K. Ismail, K. Y. Lee, and J. O. Chu, "Weak localization in backgated $Si/Si_{0.7}Ge_{0.3}$ quantum-well wires fabricated by reactive ion etching," Phys. Rev. B **54**, 10604–10608 (1996).
[59]I. B. Berkutov *et al.*, "Interference effects in silicon-germanium heterostructures with quantum wells of different widths," Low Temp. Phys. **42**, 111–118 (2016).
[60]S. Shamim *et al.*, "Dephasing rates for weak localization and universal conductance fluctuations in two dimensional Si:P and Ge:P δ-layers," Sci. Rep. **7**, 46670 (2017).